Journal of Power Sources 313 (2016) 213–222

Contents lists available at ScienceDirect

Journal of Power Sources

journal homepage: www.elsevier.com/locate/jpowsour

Development of a water based process for stable conversion cathodes on the basis of FeF_3

Alexander Pohl [a, *], Mohammadkazem Faraz [a], Andreas Schröder [a, b], Michael Baunach [b], Wilhelm Schabel [b], Alexander Guda [c], Viktor Shapovalov [c], Alexander Soldatov [c], Venkata Sai Kiran Chakravadhanula [a, d, e, f], Christian Kübel [a, d, e], Ralf Witte [a, f], Horst Hahn [a, d, f], Thomas Diemant [g], R. Jürgen Behm [d, g], Hermann Emerich [h], Maximilian Fichtner [a, d]

[a] Institute of Nanotechnology, Karlsruhe Institute of Technology, P.O. Box 3640, 76021, Karlsruhe, Germany
[b] Institute of Thermal Process Engineering, Thin Film Technology, Karlsruhe Institute of Technology, P.O. Box 3640, 76021, Karlsruhe, Germany
[c] International Research Centre "Smart Materials", Southern Federal University, Sorge 5, 344090, Rostov-on-Don, Russian Federation
[d] Helmholtz Institute Ulm, Karlsruhe Institute of Technology, Helmholtzstr. 11, 89081, Ulm, Germany
[e] Karlsruhe Nano Micro Facility, Karlsruhe Institute of Technology, P.O. Box 3640, 76021, Karlsruhe, Germany
[f] KIT-TUD Joint Laboratory Nanomaterials, Technical University Darmstadt, Jovanka-Bontschits-Str. 2, 64287, Darmstadt, Germany
[g] Institute of Surface Chemistry and Catalysis, Ulm University, Albert-Einstein-Allee 47, 89081, Ulm, Germany
[h] Swiss-Norwegian Beamline, European Synchrotron Radiation Facility, BP 220, 38043, Grenoble, France

HIGHLIGHTS

- HTB-FeF_3/rGO shows superior cyclic stability due to the microstructure.
- Iron fluoride particles are intermixed with reduced graphene oxide matrix.
- On charging, the hexagonal-tungsten-bronze FeF_3 framework is not restored.

GRAPHICAL ABSTRACT

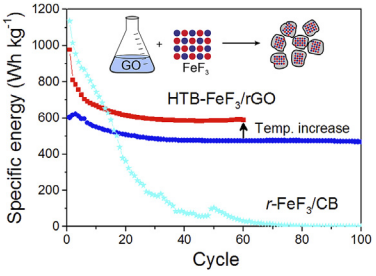

ARTICLE INFO

Article history:
Received 23 December 2015
Received in revised form
19 February 2016
Accepted 25 February 2016
Available online xxx

Keywords:
Iron fluoride
Reduced graphene oxide
Conversion material
Lithium battery
Principle component analysis
Mössbauer spectroscopy

ABSTRACT

A facile water based synthesis method for HTB-FeF_3/rGO and *r*-FeF_3/rGO composites was developed using FeF_3 nanoparticles prepared by ball-milling and aqueous graphene oxide precursor. Electrodes of HTB-FeF_3/rGO were cast in ambient air and the calendered electrode shows a stable specific energy of 470 Wh kg^{-1} (210 mA h g^{-1}, 12 mA g^{-1}) after 100 cycles in the range 1.3–4.3 V with very little capacity fading. The good cycle stability is attributed to the intimate contact of FeF_3 nanoparticles with reduced graphene oxide carbon surrounding. Using a combination of in situ XRD, XAS and ex situ Mössbauer spectroscopy, we show that during discharge of HTB-FeF_3/rGO composite Li is intercalated fast into the tunnels of the HTB-FeF_3 structure up to $x = 0.92$ Li. The Li intercalation is followed by slow conversion of HTB-Li_xFeF_3 to LiF and Fe nanoparticles below 2.0 V. During charge, the LiF and Fe phases are slowly transformed to amorphous FeF_2 and FeF_3 phases without reformation of the HTB-FeF_3 framework

* Corresponding author. Karlsruhe Institute of Technology, Institute of Nanotechnology, Hermann-von-Helmholtz Platz 1, 76344, Eggenstein-Leopoldshafen, Germany.
E-mail address: alexander.pohl@kit.edu (A. Pohl).

http://dx.doi.org/10.1016/j.jpowsour.2016.02.080

structure. At an elevated temperature of 55 °C a much higher specific energy of 780 Wh kg^{-1} was obtained.

1. Introduction

The energy density (gravimetric and volumetric) of fossil fuels such as gasoline, diesel and, when extracted from natural gas also hydrogen, is about 50–100 times higher than that of current Li-ion, NiMH and lead acid batteries [1]. This explains why it is tremendously difficult to develop full cell battery electric vehicles (BEVs), which have the same or nearly the same driving range (800–1200 km) than that of traditional automobiles based on the internal combustion engine. Recently, the US department of energy has defined a new target for electrochemical storage devices for automotive applications [2]. For a car to reach a driving range of 300 miles (ca. 480 km), the battery needs to have an energy density of 250 Wh kg^{-1} at system level, which is 2.5 times higher than state-of-the-art battery packs currently in use for BEVs [3]. After taking losses related to the electrode formulation (binder, carbon additives), electrode casting (thickness of active layer and current collector, porosity), cell construction (prismatic, pouch or round) and battery stack assembly (battery management, cooling etc.) into account, the electrode material is required to have a practical energy density of 700–800 Wh kg^{-1} at high C-rates.

Conversion materials, with the general formula $M^{n+}X_n + n\cdot e^- + n\cdot Li^+ \leftrightarrows M^0 + n\cdot LiX$ and the ability to transfer more than one electron per transition metal unit M ($n > 1$), are considered as next generation high capacity cathode materials [3,4]. In a conversion material, M is usually a 3*d* transition metal and X^{n-} an anion such as H^-, O^{2-}, F^-, S^{2-} and Se^{2-} [5]. The battery is usually constructed in the charged state and on discharge, the metal fluoride, metal oxide etc. is transformed into metal nanoparticles M^0 dispersed in an insulating matrix of LiX [6]. Conversion materials based on metal fluorides are particularly interesting, because of the strong M–F bond, some of them such as FeF_3, CoF_3, NiF_3 and CuF_2 have a high operating voltage (>2.5 V) suitable as cathodes [7]. Among the fluorides, iron fluoride has the highest theoretical energy density of 1950 Wh kg^{-1} (2.74 V, 712 mA h g^{-1}) and is non-toxic, environmentally friendly, cheap and abundant [8].

Traditionally, FeF_3/C composites have been prepared by ball-milling commercial rhombohedral FeF_3 with carbon black to reduce the primary particle size and to coat the *r*-FeF_3 nanoparticles with an electrically conducting layer of carbon [9,10]. This approach leads to materials with large initial capacity up to the theoretical maximum of 712 mA h g^{-1}, but poor cycle stability as the carbon coating is incomplete and not attached strongly enough to the FeF_3 particle surface. The carbon shell "peels off" during prolonged cycling due to pulverisation of the electrode (repeated formation of Fe/LiF phases). Later, $FeF_3\cdot nH_2O$ nanoparticles have been prepared by a liquid phase method using HF and combined with acetylene black [11–13], activated carbon [14], CNTs [15] and graphene [16,17] to obtain $FeF_3\cdot nH_2O$/C composites. However, most composites prepared via liquid phase method worked well in the Li-intercalation range 2.0–4.5 V, but showed poor cycle stability in the conversion range 1.0–4.5 V. To improve cycle stability, graphene oxide has been recently utilised in a number of publications to enable *r*-FeF_3/rGO composite materials with strong FeF_3/carbon interactions [8,18–22]. For example, Liu et al. [19] have prepared a *r*-FeF_3/rGO composite consisting of in situ grown $FeF_3\cdot 3H_2O$ anchored on HF-etched graphene sheets. After removal of water, the *r*-FeF_3/rGO composite shows a remarkably high capacity of 210 mA h g^{-1} when cycled between 2.0 V and 4.5 V (C/5) and 490 mA h g^{-1} when cycled in the range 1.5–4.5 V (C/10). The good cycle performance of this composite can be attributed to the high electronic conductivity and the low ionic resistance of the graphene sheets. Using a facile self-assembly approach, Zhao et al. [18] have prepared free-standing *r*-FeF_3/rGO paper from FeF_3 nanoparticles and graphene oxide water suspension followed by photothermal reduction. The ability to self-assemble the *r*-FeF_3/rGO paper was attributed to attracting forces of FeF_3 nanoparticles, which are strongly hydrophilic and have a positive surface charge (zeta potential = 34(1) mV) and negatively charged graphene oxide suspension (zeta potential = −57(5) mV). The free-standing *r*-FeF_3/rGO paper used directly as cathode shows initial high capacity of 587 mA h g^{-1} (20 mA g^{-1}), but cycle stability is poor with quick capacity fading after 20 cycles due to the special architecture of the free-standing *r*-FeF_3/rGO paper.

Iron-fluoride based nanomaterials with orthorhombic hexagonal-tungsten-bronze (HTB) structure were reported by Li and co-workers [23–27] and prepared using a non-aqueous approach in an ionic liquid medium. The HTB-$FeF_3\cdot 0.33H_2O$ material shows an interesting sponge-like morphology with needles on the surface and high Li-ion mobility. When considered as Li-intercalation host, HTB-$FeF_3\cdot 0.33H_2O$ can store up to 0.66 Li per formula unit (156 mA h g^{-1}) and a reversible capacity of 130 mA h g^{-1} was observed in the range 1.6–4.5 V [23]. The stability of the HTB-$FeF_3\cdot 0.33H_2O$ framework structure towards Li insertion was attributed to the presence of zeolitic water in the channels.

In this work, we developed a facile water based synthesis method to produce HTB-FeF_3/rGO (and *r*-FeF_3/rGO) nanocomposites using aqueous graphene oxide suspension and FeF_3 nanoparticles. The detailed charge/discharge mechanism in HTB-FeF_3/rGO was investigated using simultaneous in situ X-ray absorption spectroscopy (XAS) above the Fe K-edge, X-ray diffraction (XRD) and ex situ Mössbauer spectroscopy. The combination of such methods determines unambiguously the charge state of Fe, the life cycle of initial crystalline HTB-FeF_3 phase and the Fe local surrounding [28–30].

2. Experimental

2.1. Synthesis of graphene oxide

Graphene oxide (GO) was used as a precursor for FeF_3/rGO composite materials and prepared from natural graphite flakes using a modified Hummer's method as described previously [18]. Details of the synthesis procedure are given in the Supporting Information.

2.2. Synthesis of HTB-FeF_3/rGO and r-FeF_3/rGO composites

The FeF_3/rGO composite materials were prepared by using ball-milled FeF_3 and aqueous GO suspension followed by thermal reduction. In a typical synthesis, FeF_3 (3.0 g, Alfa Aesar, 98%) was placed in a WC milling vial inside an argon filled glove box and milled with a ball-to-powder ratio of 60 at 150 rpm for 20 h using a

Table 1
Synthesis conditions. Pre BM: ball-milling of FeF_3 before mixing with GO suspension; post BM: additional ball-milling of composite material after grinding; reduction temperature and time; ICP-OES elemental concentrations of Fe and S; calculated FeF_3 (taking phase fractions and lattice water into account) and rGO carbon assuming the remaining element is carbon.

No.	Pre BM	Post BM	Temp. °C	Time h	Fe wt %	S wt %	FeF_3 wt %	C wt %
1	–	–	300	4	32.2	6.6	65.1	28.4
2	x	–	200	12	40.0	2.7	84.0	13.3
3[a]	x	x	200	12	38.5	2.3	78.6	19.1

[a] Repetition of sample **2**.

Fritsch Pulverisette 6 planetary mill. Ball-milled FeF_3 (4.5 g) was dispersed in deionised water (60 mL) using an ultrasonic bath. The FeF_3/water suspension was added to GO suspension (300 mL) and stirred for 5 min. The suspension thickened after merging of the two liquids. The water was removed at 60 °C under vacuum with a rotary evaporator until completely dry. The black residue was reduced at 200–300 °C under argon mixed with 5 wt % H_2 for 4–12 h inside a tube furnace followed by a natural cool down to room temperature. The black residue was mortared into a fine black powder followed by mild ball-milling (150 rpm, 20 min). Details of the synthesis procedure of samples **1**–**3** are given in Table 1. For the structural study, the procedure of sample **2** was repeated to obtain more material.

2.3. Physical characterisation

The elemental concentrations of Fe and S were determined using inductive coupled plasma–optical emission spectroscopy (ICP-OES). Laboratory powder X-ray diffraction patterns were collected using a STOE Stadi P diffractometer equipped with a Dectris Mythen 1 K linear silicon strip detector and Ge(111) double crystal monochromator (Mo $K_{\alpha 1}$, $\lambda = 0.7093$ Å) in Debye-Scherrer geometry. Samples were filled into 0.7 mm borosilicate capillaries and data collected between 3 and 63° 2θ. The mass fractions of crystalline phases were determined by the Rietveld method using the TOPAS-Academic software [31]. Mössbauer spectra were recorded using a constant acceleration-type spectrometer in transmission geometry with a moving source of ^{57}Co in a Rh matrix. Approximately 50 mg material was sealed into a plastic bag inside an argon filled glove box. The isomer shift is given relative to α-Fe at room temperature.

2.4. Morphological characterisation

SEM micrographs were recorded at 10 kV using a Zeiss Leo-1530 scanning electron microscope (InLens detector) equipped with an Oxford Instruments X-max^N EDX detector. TEM characterisation was carried out using an aberration image corrected FEI Titan 80–300 transmission electron microscope equipped with a Gatan imaging filter (Tridiem 863) operated at 80 kV. Samples were prepared by dispersing a small amount of powder onto holey carbon Au grids (Quantifoil) inside an argon filled glove box and transferred under Ar to the sample chamber using a Gatan vacuum transfer holder.

Table 2
Rietveld refinement parameters. *r*-FeF_3 and HTB-$FeF_3 \cdot nH_2O$ phase fractions; refined oxygen occupancy and water content n; refined lattice parameters of main FeF_3 phase. Literature data: *r*-FeF_3: $a = 5.362$ Å, $\alpha = 57.94°$ [53], HTB-$FeF_3 \cdot 0.33H_2O$: $a = 7.423$ Å, $b = 12.730$ Å, $c = 7.526$ Å [43].

No.	*r*-FeF_3 wt %	HTB-FeF_3 wt %	O occ., nH_2O	Ref. LP's Å, °
1	89(1)	11(1)	–	*a*: 5.3558(5) α: 58.098(7)
2	11.5(4)	88.5(4)	0.84(1), 0.28	*a*: 7.384(3) *b*: 12.780(5) *c*: 7.5339(5)
3[a]	20.9(4)	77.1(4)	0.26(1), 0.09	*a*: 7.397(1) *b*: 12.761(2) *c*: 7.5412(6)

[a] Repetition of sample **2**.

2.5. Electrochemical characterisation

Galvanostatic charge/discharge experiments of FeF_3/rGO cathodes vs. Li-metal anode were performed using Swagelok-type cells and CR2032 coin cells. For Swagelok cells, the powders were mixed with 10 wt % carbon black and used directly without casting. For coin cells, a slurry was prepared and the material cast onto Al foil. Details of the electrode preparation are given by Baunach et al. [32] and in the Supporting Information. Batteries were tested using an Arbin Instruments BT2000 galvanostat in the voltage range 1.3–4.3 V.

2.6. In situ XAS/XRD characterisation

Simultaneous X-ray absorption spectra and diffraction patterns were recorded in situ at the Swiss-Norwegian Beamline (BM01B) of the European Synchrotron Radiation Facility (ESRF), Grenoble, France. The home-built battery cells with glassy carbon windows transparent for X-rays were constructed as described previously

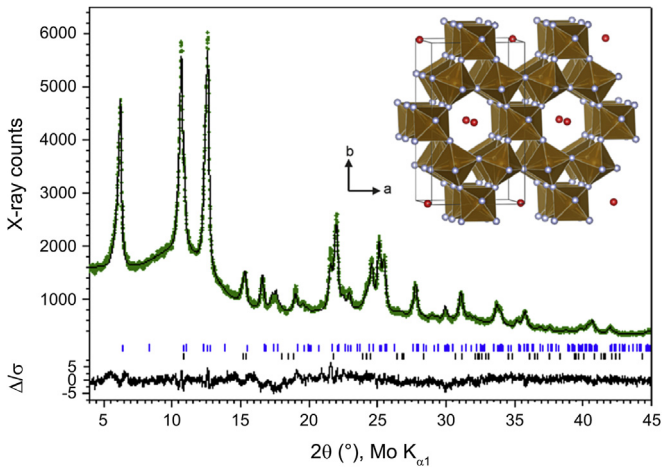

Fig. 1. Rietveld refinement of HTB-FeF_3/rGO (**2**) composite ($\lambda = 0.7093$ Å). The green dots correspond to experimental data, the black line is the calculated fit. The blue and black tick marks are at the Bragg positions of HTB-$FeF_3 \cdot 0.28H_2O$ and *r*-FeF_3 phases, respectively. The inset shows the HTB-FeF_3 structure [43] with hexagonal tunnels along the *c*-axis filled 1/3 with water molecules (red spheres). (For interpretation of the references to colour in this figure legend, the reader is referred to the web version of this article.)

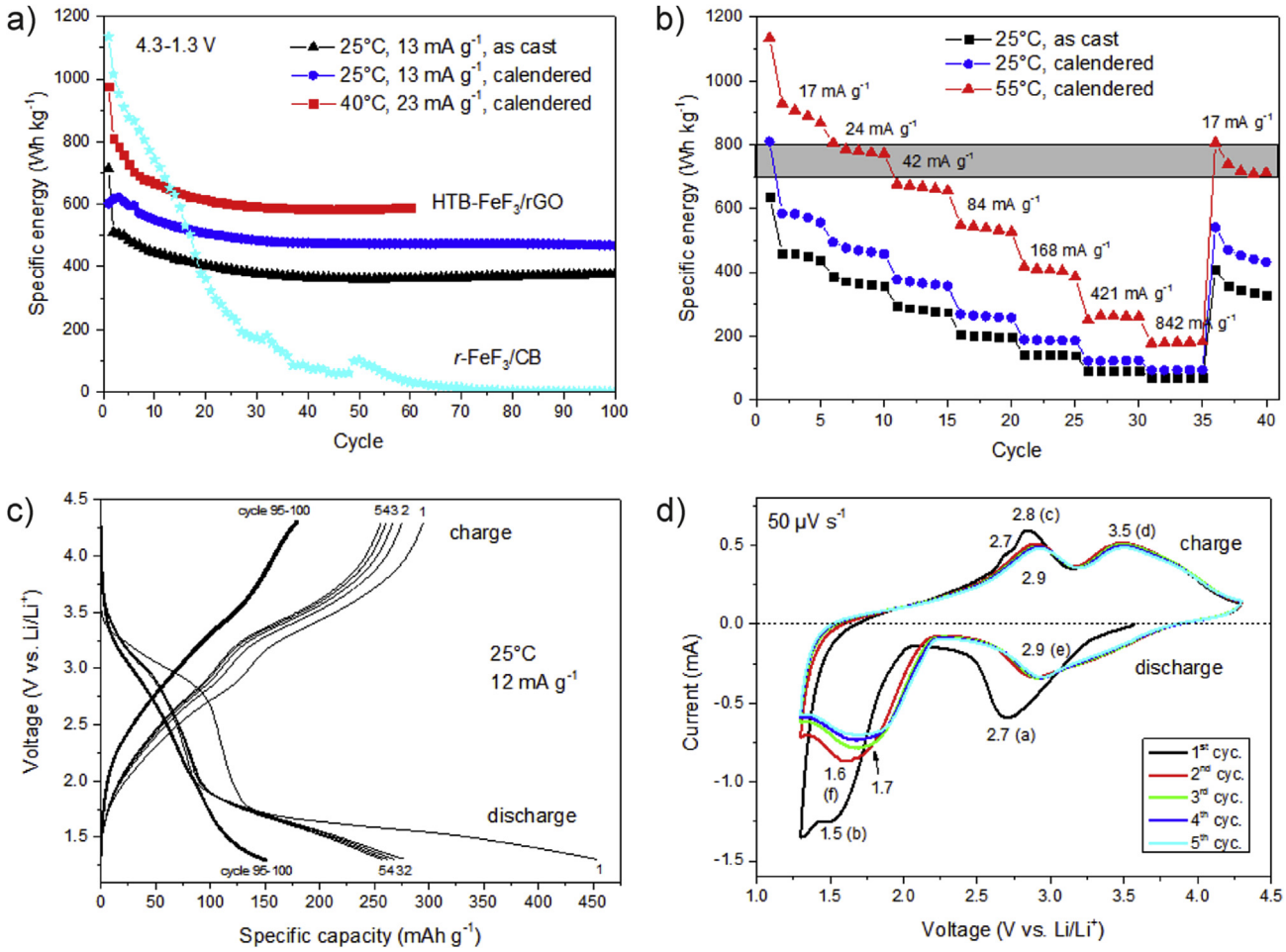

Fig. 2. Electrochemical performance of HTB-FeF_3/rGO (**2**). a) Cyclic stability of as cast and calendered films in coin cells at 25 °C and 40 °C in comparison with FeF_3 ball-milled with carbon black. b) Rate capability test of as cast and calendered films at 25 °C and 55 °C. The grey bar indicates the target of 700–800 Wh/kg on materials level [3]. c) Galvanostatic profile and d) cyclic voltammogram of powder in a Swagelok cell with reference to charge/discharge regions defined in Fig. 4.

[28]. Two cells were installed in parallel on a rotational stage and galvanostatic charge/discharge curves recorded using Gamry Interface 1000 potentiostats with a constant current of 50 µA. On each cell, diffraction was recorded for 15 min followed by Fe K-edge absorption for 20 min, then the stage was turned 180° for the other cell and data collection resumed. Ten 2D diffraction images were recorded with 5 s acquisition time by the CMOS-Dexela 2D detector. Both the wavelength $\lambda = 0.50574$ Å and the sample-to-detector distance of 324.05 mm were calibrated using LaB_6 and silicon powder standards. Subsequent averaging and integration were carried out using Fit2D software [33]. Fe K-edge X-ray absorption spectra were measured in transmission mode employing a Si(111) monochromator in continuous scanning mode. Ionization chambers were used to monitor intensity before and after the sample and a Fe foil was measured simultaneously with the sample as a reference compound to monitor a possible energy drift.

2.7. Theoretical methods

The series of Fe K-edge XANES spectra collected at different voltages were mathematically decomposed into spectra representing phases formed during charge/discharge using principle component analysis (PCA) [34] as implemented into FitIt software [35]. The concentrations of the components and spectra itself were determined using physical constraints: spectra should be normalized, the values of concentrations should be positive, two of three components under consideration should represent initial FeF_3 state and final Fe state of composite material.

3. Results and discussion

The HTB-FeF_3/rGO and *r*-FeF_3/rGO composites were synthesised using an aqueous graphene oxide water suspension and commercial FeF_3 as described in the experimental section. Depending on the synthesis conditions (pre ball-milled vs. as received FeF_3, temperature, grinding of composite vs. additional ball-milling), the composites contained a mixture of rhombohedral FeF_3 and hexagonal-tungsten-bronze-type HTB-FeF_3 polymorphs with varying weight fractions and a small amount of WC (<1 wt %) introduced by abrasion during ball-milling (Table 2). Using pre ball-milled nanocrystalline FeF_3, the majority of *r*-FeF_3 was transformed to HTB-FeF_3, whereas using the *r*-FeF_3 as received, the amount of HTB-FeF_3 in the composites was much less. The water based graphene oxide process is scalable, HF-free and depending on the concentration of GO suspension, composites with a variable amount of 13–28 wt% reduced graphene oxide (rGO) were produced. This is an advantage, as the optimal carbon content is fine-tuneable for production of a commercial material with an optimal electrical conductivity and gravimetric capacity. The HTB-FeF_3 structure has large hexagonal channels along the *c*-axis which can

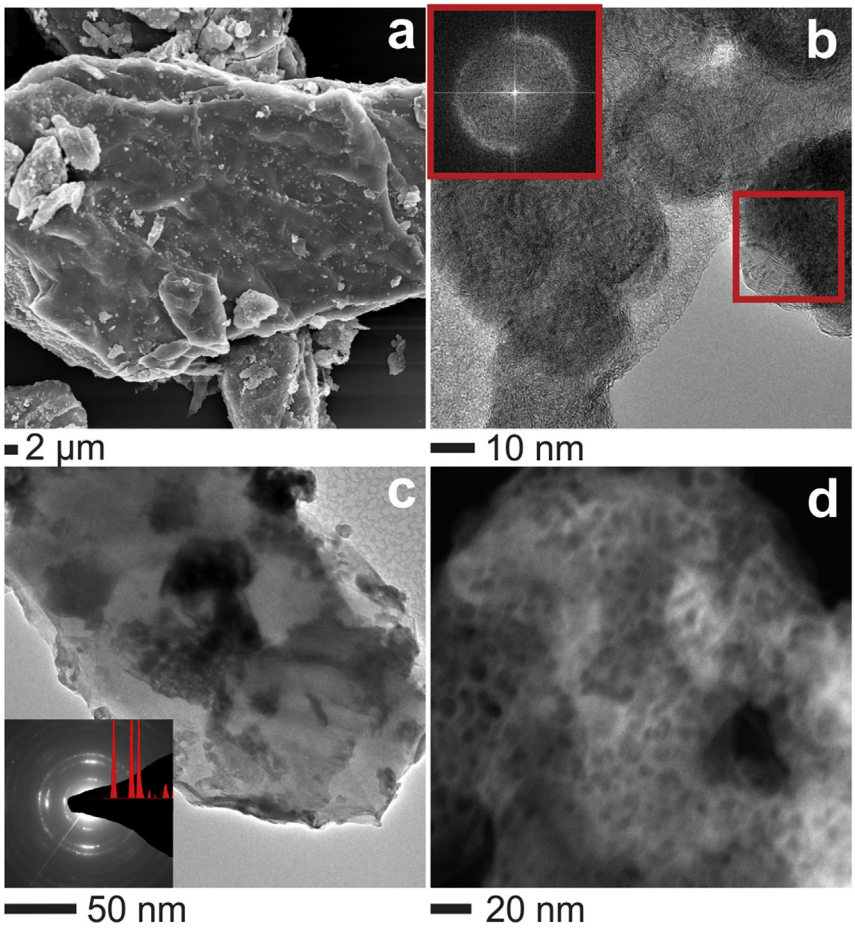

Fig. 3. Morphology of HTB-FeF_3/rGO (**2**) composite. a) SEM micrograph showing FeF_3 particles and rGO carbon. b) HR-TEM micrograph of reduced graphene oxide (rGO) with FFT pattern of rGO in inset ($d = 3.5$ Å). c) Brightfield TEM image of FeF_3 particles (dark) embedded in rGO carbon. The SAED pattern (inset) shows a diffractogram matching reflections of the HTB-FeF_3 structure. d) HAADF STEM image of a selected microporous FeF_3 particle with an average pore diameter of $d = 6$ nm.

accommodate additional lattice water (Fig. 1). Refinement of the O occupancy shows that the HTB-$FeF_3 \cdot nH_2O$ phase in composites (**2**) and (**3**) is partially dehydrated with $n = 0.28$ (**2**) and $n = 0.09$ (**3**), respectively. The removal of lattice water is also indicated by a slight contraction of the *a*-axis (5.3‰ (**2**), 3.5‰ (**3**)) and expansion of the *c*-axis (1.1‰ (**2**), 2.0‰ (**3**)).

3.1. Electrochemical performance

The electrochemical performance of the composites (**1**–**3**) was found to be very similar after the first cycle irrespective of the amount of HTB-FeF_3 and *r*-FeF_3 polymorphs present. Electrodes of HTB-FeF_3/rGO (**2**) composite were prepared using a self-made batch coating machine with a custom designed slot nozzle dryer (Fig. S1, §ESI). The hygroscopic FeF_3 is well protected by the rGO carbon from ambient moisture enabling casting on the bench without affecting the performance of the electrode. This is beneficial as no special dry-room or inert gas conditions are required to produce high-quality, production-grade electrodes from these materials. The electrochemical performance of HTB-FeF_3/rGO (**2**) is shown in Fig. 2. Please note, the cyclic stability and rate capability are plotted against specific energy in order to be able to compare the performance with other classes of battery materials. Alternative plots using specific capacity are given in the Supporting Information Fig. S2. The composite was cycled at two different temperatures using as cast and calendered electrodes (Fig. 2a). After the first few initial cycles, the HTB-FeF_3/rGO composite shows excellent cycle stability compared to a *r*-FeF_3 composite prepared by ball-milling with an equivalent amount of carbon black (HTB-FeF_3 (**2**): 22 wt % total (rGO + CB); *r*-FeF: 30 wt % CB, cyan curve). The as cast HTB-FeF_3/rGO electrode shows a stable specific energy of 368 Wh kg^{-1} (166 mA h g^{-1}, 12.8 mA g^{-1}, black curve) at 25 °C for 100 cycles with negligible capacity fading after the 40th cycle. The stable cycle performance is attributed to a very firm contact of FeF_3 particles with the electron conducting reduced graphene oxide environment. The good contact is an effect of the attracting forces of the positively charged FeF_3 particle surface and negatively charged graphene oxide in water before drying [18]. Calendering the electrode increases the specific energy by 29% to 474 Wh kg^{-1} (215 mA h g^{-1}, cycle 40–100, blue curve) without affecting the long term cyclic stability due to pulverisation of small FeF_3 agglomerates present in the as cast electrode. Raising the temperature of the calendered electrode from 25 °C to 40 °C increases the specific energy further by 24% to 586 Wh kg^{-1} (277 mA h g^{-1}, 40–60 cycles, red curve) compared to the calendered electrode cycled at 25 °C. At 40 °C, the conversion rate of FeF_3 into LiF and Fe is accelerated due to higher ion mobility. However, after 60 cycles (not shown) the specific energy increases abnormally fast due to decomposition of the $LiPF_6$ electrolyte [36].

Rate capability tests of as cast and calendered HTB-FeF_3 (**2**) electrodes were performed at two different temperatures and are shown in Fig. 2b. The grey bar represents the specific energy target

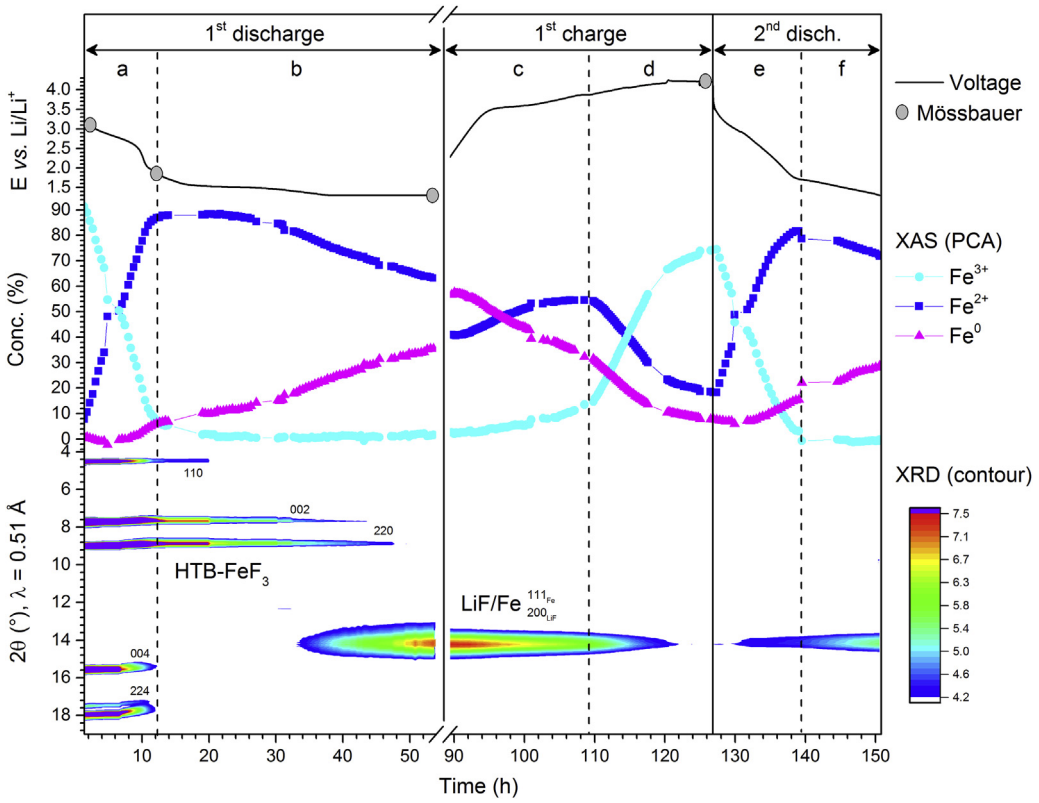

Fig. 4. In situ XAS/XRD experiment of HTB-FeF_3/rGO (**3**) composite. Top: Voltage profile during charge/discharge of the cell with grey circles indicating points where ex situ Mössbauer spectra were collected. Middle: PCA concentration profile of Fe, Fe^{2+} and Fe^{3+} components obtained from simultaneous decomposition of 260 Fe K-edge XANES spectra. Bottom: XRD contour plot (λ = 0.51 Å) showing evolution of HTB-FeF_3, LiF and Fe phases during charge/discharge.

of 700–800 Wh kg^{-1} required for practical automotive batteries [3]. Both calendering and the elevated temperature has a beneficial effect on the rate performance. The calendered electrode cycled at 55 °C shows a high average initial discharge energy of 900 Wh kg^{-1} (435 mA h g^{-1}, 17 mA g^{-1}, red curve) over cycles 2–4, which exceeds the target on materials level by 100–200 Wh kg^{-1}. When the current density is raised to 0.84 A g^{-1} (equivalent to 1.2 C), the specific energy drops considerably to 180 Wh kg^{-1} (80 mA h g^{-1}). Compared to the fast Li-ion diffusion into the HTB-FeF_3 tunnel structure and other Li-intercalation host materials such as NMC, the conversion of HTB-Li_xFeF_3 to LiF/Fe nanoparticles is slow leading to a kinetic limitation of the material. After changing the discharge current back to its initial value of 17 mA g^{-1}, the calendered electrode lost 19% of its initial capacity due to degradation of electronic as well as ionic contact within the electrode.

The galvanostatic charge/discharge profile shown in Fig. 2c resembles that of HTB-FeF_3 in the first cycle and amorphous FeF_3 in subsequent cycles as will be shown later. In the first cycle, there is a short plateau above 2.8 V where Li intercalation into the HTB-FeF_3 tunnel structure takes place [23,24] followed by a sloping region above 2 V and a long plateau due to conversion of HTB-Li_xFeF_3 into LiF and Fe nanoparticles. In summary, the overall conversion reaction can be written as $FeF_3 + 3 \cdot e^- + 3 \cdot Li^+ \leftrightarrows Fe^0 + 3 \cdot LiF$ leading to a theoretical capacity of 712 mA h g^{-1} (1950 Wh kg^{-1}) for the 3 electron transfer. There is a large irreversible capacity loss of 135 mA h g^{-1} in the first cycle due to formation of a solid electrolyte interface on the Li-metal anode [37] or because of as yet unidentified reactions of the FeF_3 cathode with the electrolyte. After complete discharge, the HTB-FeF_3 is transformed into Fe metal nanoparticles embedded into an insulating matrix of LiF nanocrystallites [6]. In subsequent cycles, the discharge plateau above 2.8 V is shortened considerably due to collapse of the HTB tunnel structure and subsequent formation of amorphous FeF_3, which has less capacity for Li storage than the HTB framework structure.

The CV diagram in Fig. 2d clearly shows that the charge/discharge mechanism in the first cycle (black) differs from the storage mechanism in subsequent cycles (letters **a**–**f** correspond to regions defined in Fig. 4). In the first cycle, the intercalation region **a** has a pronounced discharge peak with a maximum at 2.7 V. In subsequent cycles, peak **e** is shifted from 2.7 V to 2.9 V and is much broader compared to the first cycle indicating a solid solution or surface charge storage mechanism rather than an intercalation process. The conversion regimes **b** and **c** are characterised by a large voltage hysteresis of approximately 1.2 V due to the phase transformations [38].

3.2. Microstructure

The microstructure of HTB-FeF_3/rGO (**2**) was investigated using SEM, TEM and BET. The SEM image in Fig. 3a shows a large HTB-FeF_3/rGO particle with a textured surface covered by smaller HTB-FeF_3/rGO particles. EDX analysis (Fig. S3, §ESI) shows a strong overlap between C, O, S and F elemental maps indicating that HTB-FeF_3 particles are intermixed with rGO. The graphene oxide contains 2–7 wt % sulphur due to incomplete removal of sulphuric acid [39] as determined by ICP-OES (Table 1) and XPS (Fig. S4, §ESI). The C_{1s} XPS spectrum of *r*-FeF_3/rGO (**1**) consists of the same carbon functionalities found for graphene oxide [40], but with reduced intensities of the C–O and C=O peaks indicating partial deoxygenation by the reduction process. The HR-TEM micrograph (Fig. 3b) shows an onion-like graphitic carbon morphology. The graphitic layers have an interlayer spacing of d = 3.5 Å, which is in

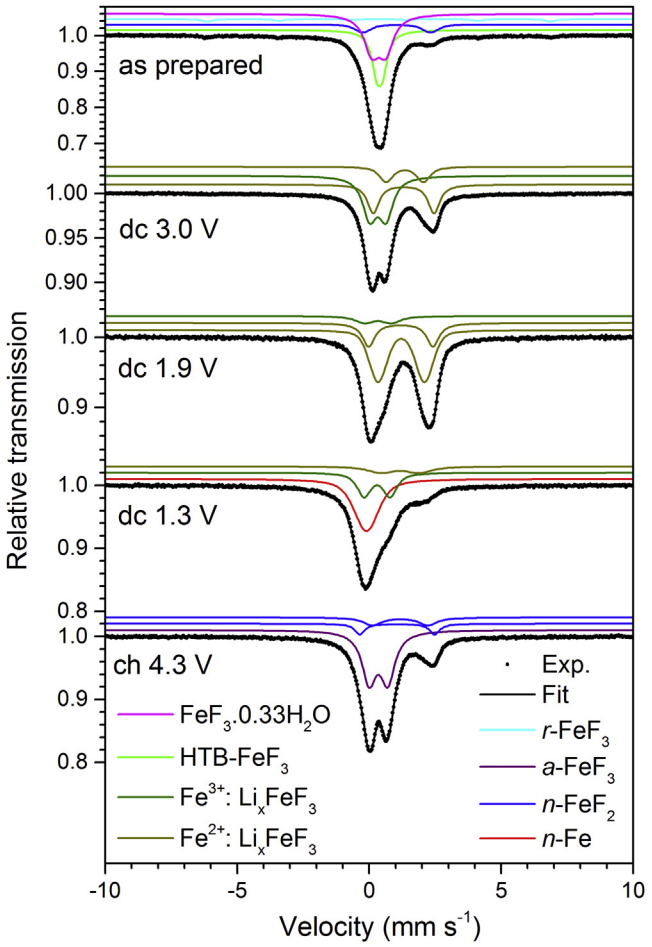

Fig. 5. Mössbauer spectra of as prepared HTB-FeF_3/rGO (**3**) composite, discharged to 3.0 V, 1.9 V and 1.3 V and charged to 4.3 V. The experimental spectrum is given as black dots and the total fit as a black line. Components of the fit are shown as coloured lines above the spectrum.

good agreement with the *d*-spacing of reduced graphene oxide [41] (but larger than $d = 3.356(4)$ Å reported for graphite [42]). The enlarged interlayer distance is in agreement with lattice defects and residual oxygen groups on the surface which create anchor sites for FeF_3 particles. Fig. 3c shows HTB-FeF_3 nanoparticles (dark) embedded in a carbon matrix. The SAED pattern (inset) is in good agreement with the HTB-$FeF_3 \cdot 0.33H_2O$ structure [43]. A small portion of the HTB-FeF_3 particles shows mesoporosity with an average pore diameter of 6 nm (Fig. 3d and Fig. S5, §ESI). However, the BET surface area of 20.1 m^2/g and the cumulative pore volume of 0.04 cm^3/g (Fig. S6, §ESI) are small for a truly "porous" material indicating that the majority of HTB-FeF_3 particles exist as a dense solid phase. These dense particles are not accessible by N_2 molecules in BET measurements, but are involved in the Li diffusion process during intercalation and conversion reactions. The combined TGA/DSC/MS analysis (Fig. S7, §ESI) shows that the HTB-FeF_3/rGO (**2**) composite is thermally stable in air up to 300 °C.

3.3. Reaction mechanism

To investigate Fe oxidation state changes and the phases formed during intercalation and conversion of HTB-FeF_3/rGO, we collected simultaneous in situ synchrotron X-ray absorption and X-ray diffraction data and ex situ laboratory Mössbauer spectra at certain points in the first and beginning of second cycle. Fe K-edge XANES

Table 3
Ex situ Mössbauer parameters of HTB-FeF_3/rGO (3) during charge/discharge. Isomer shift (IS), quadrupole splitting (QS), Lorentzian linewidth (Γ) and hyperfine splitting (B_{HF}). IS relative to α-Fe. Reported values for known iron fluorides are given for comparison.

State[a] V	IS mm s^{-1}	QS mm s^{-1}	Γ mm s^{-1}	B_{HF} T	Area %
As prep.	0.47(1)	0.54(18)	0.67(10)	–	61.9
	0.50(2)	0.22(2)	0.46(7)	–	28.0
	1.14(2)	2.56(3)	0.4	–	7.0
	0.46(1)	0.01(3)	0.41(5)	40.4(1)	3.0
3.0	0.33(3)	0.62(5)	0.598(6)	–	57.8
	1.305(5)	2.300(9)	0.49(1)	–	28.0
	1.35(8)	1.4(2)	0.45(5)	–	14.2
1.9	1.321(2)	1.76(2)	0.31(4)	–	46.0
	1.302(2)	2.434(6)	0.56(2)	–	33.9
	0.43(1)	1.02(1)	0.81(3)	–	20.0
1.3	0	–	0.70(2)	–	55.5
	1.27(4)	1.45(7)	1.10(3)	–	23.3
	0.405(4)	0.979(6)	0.5	–	21.2
4.3	0.456(2)	0.709(4)	0.649(2)	–	75.0
	1.279(7)	2.11(2)	0.78(2)	–	17.3
	1.167(4)	2.83(1)	0.44(2)	–	7.7
$FeF_3 \cdot 0.33H_2O$ [43]	0.439(2)	0.640(4)	0.50(1)	–	–
HTB-FeF_3[b] [44]	0.400(5)	0.58(2)	0.49(4)	–	61(5)
	0.419(5)	0.23(2)	0.36(4)		39(5)
r-FeF_3 [45]	0.474(6)	0.05(1)	0.246	40.4(2)	–
a-FeF_3 [54]	0.48	0.58	0.45	–	–
FeOF [55]	0.397	1.18	–	–	–
FeF_2 [56]	1.37	2.78	0.23	–	–
n-FeF_2 [46]	1.289_{bulk}	2.733	0.352	–	75
	$1.267_{int.}$	1.968	0.550		25

[a] *r*: rhombohedral; *n*: nanocrystalline; *a*: amorphous.
[b] IS converted from 100 K to 300 K [57].

and Mössbauer spectra unambiguously determine the oxidation state of Fe, and are able to provide structural information when compared to literature data and theoretical simulations. On the other hand, XRD is able to detect changes in the long-range order as Li is intercalated. Fig. 4 shows the voltage profile with points where ex situ Mössbauer spectra have been collected, the Fe concentration profile calculated from the Fe K-edge XANES spectra using principle component analysis (PCA), and a contour plot of X-ray diffraction data. All XANES spectra were decomposed by the PCA method into three subspectra, which correspond to Fe, FeF_2 and FeF_3 phases (Fig. S8, §ESI). Best guess structural phases determined with each technique will be discussed in the following paragraphs.

Before cycling, the as prepared HTB-FeF_3/rGO (**3**) composite consists mainly of HTB-FeF_3 with hexagonal tungsten bronze structure and large hexagonal channels along the *c*-axis (Fig. 1). The channels are almost completely dehydrated (0.09 H_2O) and there is space to accommodate further Li atoms in the tunnels [24]. The XAS spectrum shows a Fe^{3+} oxidation state and the spectrum resembles that of FeF_3. However, the local structures of *r*-FeF_3 and HTB-FeF_3 consist of very similar corner-sharing FeF_6 octahedra and cannot be easily distinguished by XAS. The Mössbauer spectrum (Fig. 5) of as prepared HTB-FeF_3/rGO (**3**) composite shows two doublets, one with a larger quadrupole splitting (QS) of 0.5(2) mm s^{-1} and one with a smaller QS of 0.22(2) mm s^{-1} (Table 3). The large Fe^{3+} doublet is in good agreement with the fully hydrated structure HTB-$FeF_3 \cdot 0.33H_2O$ with 1/3 water in the channels [43]. The small Fe^{3+} doublet is due to the partial removal of H_2O molecules from the channels and, as has been observed by XRD, represents the partially dehydrated HTB-FeF_3 structure reported by Calage et al. [44]. The Mössbauer spectrum also indicates the presence of a small amount of *r*-FeF_3 (3 area %) with a large magnetic hyperfine splitting of 40.4 T in agreement with the XRD refinement (Table 2) [45]. Additionally, there is a Fe^{2+} component (7% area) with an isomer shift of 1.14(2) mm s^{-1} and a large QS of 2.56(3) mm s^{-1}. These

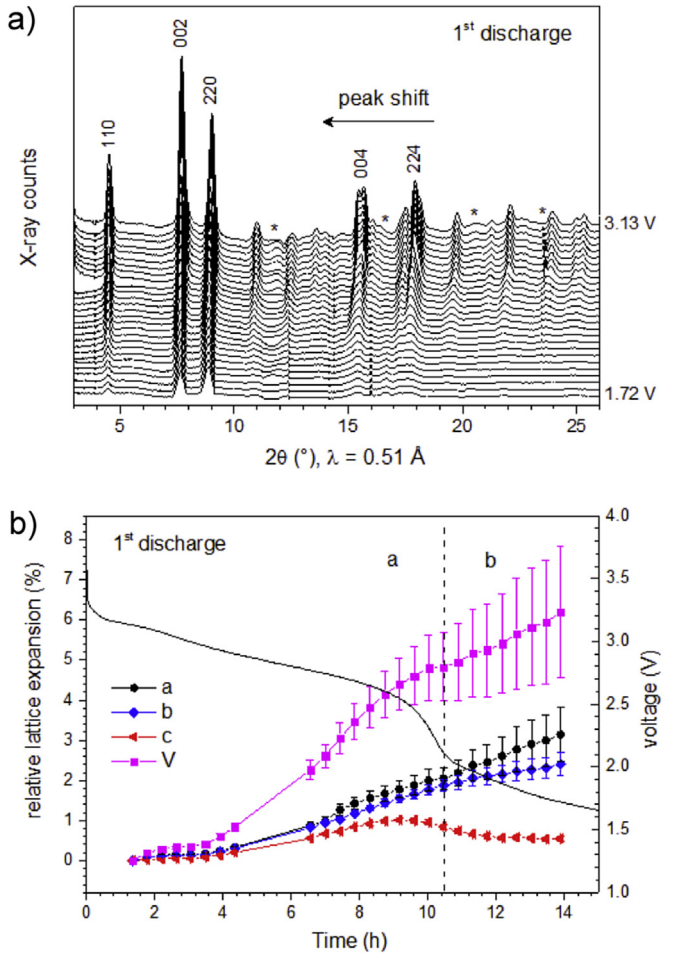

Fig. 6. a) In situ X-ray diffraction patterns of HTB-FeF_3/rGO (**3**) composite collected during first discharge showing a peak shift due to Li intercalation into HTB-FeF_3. Li reflections (*) have been excluded for clarity. b) Relative lattice expansion calculated from refined lattice parameters of HTB-Li_xFeF_3 phase.

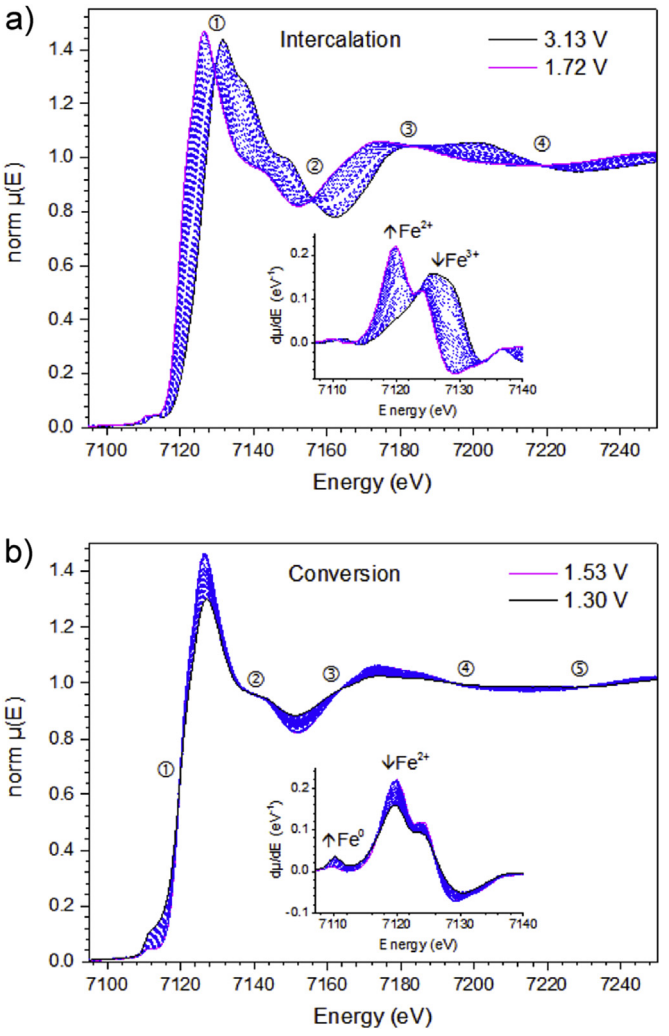

Fig. 7. In situ Fe K-edge XAS spectra of HTB-FeF_3/rGO (**3**) showing a) Li-intercalation with characteristic isosbestic points (marked with numbers 1–4). The inset shows the derivative spectra with increasing Fe^{2+} and decreasing Fe^{3+} peak intensity. b) Conversion of HTB-FeF_3 into LiF and Fe indicated by a second set of isosbestic points.

parameters suggest some form of nanocrystalline FeF_2 [46], and it is known that *r*-FeF_3 is not stable under high-energy ball-milling conditions and tends to partially reduce to FeF_2 [47]. However, the particle size of FeF_2 must be very small as no additional macroscopic FeF_2 phase was identified in the XRD pattern.

During discharge (Fig. 4, regions **a**, **b**), Li is intercalated into the HTB-FeF_3 structure up to a voltage of 2.0 V as has been observed previously [24], and is subsequently transformed into LiF and Fe nanoparticles when discharging to the cut-off voltage of 1.3 V. During the Li intercalation process (region **a**), reflections of HTB-FeF_3 shift to lower 2θ values with a corresponding unit cell volume expansion of approx. 5% (Fig. 6). The cell expansion is fairly linear (with time) up to the end of the voltage plateau at 2.5 V, which is in agreement with a topotactical Li-insertion process described by Vegard's law [48]. The XAS spectra of the Li-intercalation process (Fig. 7a) show four isosbestic points characteristic for a two phase mixture consisting of HTB-FeF_3 and HTB-Li_xFeF_3. At the end of the intercalation process, the Fe^{3+} peak (inset Fig. 7a) has almost entirely disappeared and the iron atoms are mainly in a Fe^{2+} state corresponding to a fully intercalated HTB-Li_xFeF_3 structure. From the Fe^{3+} consumption at the end of region **a** (Fig. 4, PCA) we calculated that $x = 0.92$ Li, which is much larger than the maximum of 0.66 Li for HTB-$FeF_3 \cdot 0.33H_2O$ found by the Maier group [24]. We think this is possible because in the partially dehydrated HTB-$FeF_3 \cdot 0.09H_2O$ structure, there is more room for Li atoms available compared to HTB-$FeF_3 \cdot 0.33H_2O$ with 1/3 of the channels already occupied by water molecules. The Mössbauer spectra (Fig. 5) collected in the middle and end of region (**a**) (3.0 V and 1.9 V, respectively), show a number of Fe^{2+} and Fe^{3+} doublets, which cannot be assigned unambiguously to any known iron fluoride phases. As XRD provides clear evidence that within this voltage range the prominent mechanism is intercalation, we assume that these subspectra belong to different environments in partially lithiated HTB-Li_xFeF_3.

In the conversion regime below 2.0 V (Fig. 4, region **b**), HTB-Li_xFeF_3 converts to LiF/Fe nanoparticles as can be clearly seen by the appearance of a broad LiF/Fe peak in the XRD contour plot and from the in situ XAS spectra (Fig. 7b). The XAS spectra show another set of isosbestic points and a growing Fe^0 peak (inset) indicating two phases in equilibrium (LiF cannot be seen by Fe–K edge XAS). The PCA concentration profile (Fig. 4) shows that the cell after full discharge contains 63% Fe^{2+}, 36% Fe^0 and no Fe^{3+}. This clearly shows that the conversion of HTB-Li_xFeF_3 to LiF/Fe was not complete and is much slower compared to the fast Li-intercalation process in the beginning of discharge. A second cell, which was discharged to 1.3 V prior to the synchrotron experiment, had a

much higher Fe content of 57% Fe^0 and 41% Fe^{2+} at the end of discharge and this cell was used in subsequent charge/discharge cycles (Fig. 4, regions **c**–**f**). The ex situ Mössbauer spectrum (Fig. 5) collected after full discharge at 1.3 V shows a Fe^0 singlet due to superparamagnetic Fe nanoparticles [49,50] and two doublets for Fe^{2+} and Fe^{3+}, respectively, which are attributed to partially lithiated, unreacted HTB-Li_xFeF_3.

During charge (Fig. 4, regions **c**, **d**), the LiF/Fe nanoparticles transform reversibly to FeF_2 and FeF_3 [49,51]. The XRD diffraction data did not show any new phases during charge indicating that the FeF_2 and FeF_3 particles are nanocrystalline with domain sizes below the coherent X-ray scattering length. However, the transformation of Fe into FeF_2 and FeF_3 is clearly visible in the PCA concentration profile. In the beginning of the charge process (region **c**), the amount of Fe^{2+} increases indicating formation of FeF_2, and above 3.9 V (region **d**) the Fe^{2+} concentration decreases fast with concomitant oxidation and formation of FeF_3. The Mössbauer spectrum collected after full charge at 4.3 V (Fig. 5) shows a large Fe^{3+} doublet, which is in good agreement with an amorphous FeF_3 phase. The spectrum also contains two Fe^{2+} doublets, one with a small QS of 2.11(2) mm s^{-1} and one with a large QS of 2.83(1) mm s^{-1}, which are in good agreement with nanocrystalline FeF_2 (Table 3). This is evidence that the charge process does not go via the HTB-framework structure forming HTB-$Li_xFeF_3 \cdot nH_2O$, but rather through the formation of rutile FeF_2 and amorphous FeF_3 phases. The trace amounts of hydration water, which are released into the electrolyte upon destruction of the HTB-$FeF_3 \cdot nH_2O$ framework, lead most probably to hydrolysis of a small portion of $LiPF_6$ [52]. Liu et al. [12] have investigated the conversion mechanism of $FeF_3 \cdot nH_2O$ (n = 0, 0.33 and 3) and found that during charge the initial FeF_3 hydrates are restored. In contrast to the observation of Liu and co-workers, the hydration water in our HTB-$FeF_3 \cdot nH_2O$ phases is effectively removed during first discharge and therefore not available to reform the HTB framework.

4. Conclusion

We have synthesised HTB-FeF_3/rGO (and *r*-FeF_3/rGO) composite materials as a high energy cathode for Li-ion batteries from graphene oxide suspension and commercial FeF_3 using a HF-free and scalable preparation method. The composites consist of a phase mixture of HTB-FeF_3 and *r*-FeF_3 polymorphs depending on ball-milling conditions and temperature during reduction process. HTB-FeF_3/rGO composites show a stable discharge capacity of 400–450 mA h g^{-1} at 55 °C vs. Li metal anode and a remarkably good cyclic stability over 100 cycles. The good cycle performance was attributed to the microstructure, which consists of FeF_3 particles embedded into a matrix of graphene oxide. The close contact of hygroscopic FeF_3 particles with carbon permits the preparation of high quality electrodes without the need of moisture protection in ambient air and maintains electronic as well as Li ionic conductivity during prolonged cycling. The detailed reaction mechanism was investigated using a combination of in situ XAS, XRD and ex situ Mössbauer spectroscopy. Upon discharge, Li is inserted fast into the HTB-FeF_3 tunnel structure followed by a slow conversion reaction to LiF/Fe nanoparticles. Upon charge, LiF/Fe is slowly converted back to rutile FeF_2 and amorphous FeF_3 phases without reformation of the HTB-FeF_3 framework. The HTB-FeF_3/rGO material is able to deliver a high specific energy of 700–800 Wh kg^{-1} at elevated temperature and slow rates, but the energy density is reduced at higher rates due to kinetic limitations of the conversion reaction. A solid or liquid electrolyte suitable for cycling the material above 100 °C might be a way to improve the energy density and rate capability of HTB-FeF_3/rGO significantly.

Acknowledgements

The authors thank the European Synchrotron Radiation Facility (ESRF) for granting beam time for the in situ XAS/XRD experiment. We also thank C. Ly for providing ICP-OES analytical service at the Karlsruhe Institute of Technology (FM-VEA). A. G., A. S and V. S. thank the Ministry of Education and Science of Russia for the financial support (agreement no. 14.587.21.0002, identifier RFMEFI58714X0002). Financial support by EU-RTD "Hi-C" (Novel in situ and in operando techniques for characterization of interfaces in electrochemical storage systems) in the 7th FP, grant agreement no. 608575, is gratefully acknowledged.

Appendix A. Supporting information

Supplementary data related to this article can be found at http://dx.doi.org/10.1016/j.jpowsour.2016.02.080.

References

[1] M. Fichtner, J. Alloys Compd. 509 (2011) S529.
[2] U.S. Department of Energy, 2012 Annual Merit Review Results Report, 2012.
[3] D. Andre, S.-J. Kim, P. Lamp, S.F. Lux, F. Maglia, O. Paschos, B. Stiaszny, J. Mater. Chem. A 3 (2015) 6709.
[4] M. Fichtner, in: S.R.S. Prabaharan, M.S. Michael (Eds.), Nanotechnol. Adv. Electrochem. Power Sources, Pan Stanford Publishing Pte Ltd., Singapore, 2014, pp. 51–88.
[5] J. Cabana, L. Monconduit, D. Larcher, M.R. Palacín, Adv. Mater. 22 (2010) E170.
[6] F. Wang, H.-C. Yu, M.-H. Chen, L. Wu, N. Pereira, K. Thornton, A. Van der Ven, Y. Zhu, G.G. Amatucci, J. Graetz, Nat. Commun. 3 (2012) 1201.
[7] H. Li, P. Balaya, J. Maier, J. Electrochem. Soc. 151 (2004) A1878.
[8] D.E. Conte, N. Pinna, Mater. Renew. Sustain. Energy 3 (2014) 37.
[9] F. Badway, N. Pereira, F. Cosandey, G.G. Amatucci, J. Electrochem. Soc. 150 (2003) A1209.
[10] F. Badway, F. Cosandey, N. Pereira, G.G. Amatucci, J. Electrochem. Soc. 150 (2003) A1318.
[11] Q. Chu, Z. Xing, J. Tian, X. Ren, A.M. Asiri, A.O. Al-Youbi, K.A. Alamry, X. Sun, J. Power Sources 236 (2013) 188.
[12] L. Liu, H. Guo, M. Zhou, Q. Wei, Z. Yang, H. Shu, X. Yang, J. Tan, Z. Yan, X. Wang, J. Power Sources 238 (2013) 501.
[13] J. Tan, L. Liu, H. Hu, Z. Yang, H. Guo, Q. Wei, X. Yi, Z. Yan, Q. Zhou, Z. Huang, H. Shu, X. Yang, X. Wang, J. Power Sources 251 (2014) 75.
[14] L. Liu, M. Zhou, X. Wang, Z. Yang, F. Tian, X. Wang, J. Mater. Sci. 47 (2012) 1819.
[15] S.-W. Kim, D.-H. Seo, H. Gwon, J. Kim, K. Kang, Adv. Mater. 22 (2010) 5260.
[16] T. Bao, H. Zhong, H. Zheng, H. Zhan, Y. Zhou, Electrochim. Acta 176 (2015) 215.
[17] Y. Shen, X. Wang, H. Hu, M. Jiang, X. Yang, H. Shu, J. Power Sources 283 (2015) 204.
[18] X. Zhao, C.M. Hayner, M.C. Kung, H.H. Kung, Chem. Commun. 48 (2012) 9909.
[19] J. Liu, Y. Wan, W. Liu, Z. Ma, S. Ji, J. Wang, Y. Zhou, P. Hodgson, Y. Li, J. Mater. Chem. A 1 (2013) 1969.
[20] R.G. Ma, Z.G. Lu, C.D. Wang, H.-E.E. Wang, S.L. Yang, L.J. Xi, J.C.Y. Chung, Nanoscale 5 (2013) 6338.
[21] Q. Chu, Z. Xing, X. Ren, A.M. Asiri, A.O. Al-Youbi, K.A. Alamry, X. Sun, Electrochim. Acta 111 (2013) 80.
[22] R. Ma, Y. Dong, L. Xi, S. Yang, Z. Lu, C. Chung, ACS Appl. Mater. Interfaces 5 (2013) 892.
[23] C. Li, L. Gu, S. Tsukimoto, P. a van Aken, J. Mater. Adv. Mater. 22 (2010) 3650.
[24] C. Li, L. Gu, J. Tong, S. Tsukimoto, J. Maier, Adv. Funct. Mater. 21 (2011) 1391.
[25] C. Li, L. Gu, J. Tong, J. Maier, ACS Nano 5 (2011) 2930.
[26] C. Li, X. Mu, P.A. van Aken, J. Maier, Adv. Energy Mater. 3 (2013) 113.
[27] C. Li, C. Yin, X. Mu, J. Maier, Chem. Mater. 25 (2013) 962.
[28] A.H. Pohl, A.A. Guda, V.V. Shapovalov, R. Witte, B. Das, F. Scheiba, J. Rothe, A.V. Soldatov, M. Fichtner, Acta Mater. 68 (2014) 179.
[29] F. Wang, S. Kim, D.-H. Seo, K. Kang, L. Wang, D. Su, J.J. Vajo, J. Wang, J. Graetz, Nat. Commun. 6 (2015) 6668.
[30] L. Li, Y.K. Chen-Wiegart, J. Wang, P. Gao, Q. Ding, Y.-S. Yu, F. Wang, J. Cabana, J. Wang, S. Jin, Nat. Commun. 6 (2015) 6883.
[31] A.A. Coelho, TOPAS-academic V4.1, Coelho Software, Brisbane, Australia, 2007.
[32] M. Baunach, S. Jaiser, S. Schmelzle, H. Nirschl, P. Scharfer, W. Schabel, Dry. Technol. 3937 (2015), http://dx.doi.org/10.1080/07373937.2015.1060497.
[33] A.P. Hammersley, S.O. Svensson, M. Hanfland, A.N. Fitch, D. Hausermann, High Press. Res. 14 (1996) 235.
[34] A.M. Beale, M.T.T. Le, S. Hoste, G. Sankar, Solid State Sci. 7 (2005) 1141.
[35] G. Smolentsev, A.V. Soldatov, Comput. Mater. Sci. 39 (2007) 569.
[36] A. Hofmann, M. Migeot, E. Thißen, M. Schulz, R. Heinzmann, S. Indris, T. Bergfeldt, B. Lei, C. Ziebert, T. Hanemann, ChemSusChem 8 (2015) 1892.
[37] J. Illig, Physically Based Impedance Modelling of Lithium-ion Cells, KIT Scientific Publishing, Karlsruhe, 2014.

[38] J.K. Ko, K.M. Wiaderek, N. Pereira, T.L. Kinnibrugh, J.R. Kim, P.J. Chupas, K.W. Chapman, G.G. Amatucci, ACS Appl. Mater. Interfaces 6 (2014) 10858.
[39] Y. Hong, Z. Wang, X. Jin, Sci. Rep. 3 (2013) 1.
[40] S. Stankovich, R.D. Piner, X. Chen, N. Wu, S.T. Nguyen, R.S. Ruoff, J. Mater. Chem. 16 (2006) 155.
[41] S.H. Huh, S.-H. Choi, H.-M. Ju, D.-H. Kim, J. Korean Phys. Soc. 64 (2014) 615.
[42] P. Trucano, R. Chen, Nature 258 (1975) 136.
[43] M. Leblanc, G. Ferey, P. Chevallier, Y. Calage, R. De Pape, J. Solid State Chem. 47 (1983) 53.
[44] Y. Calage, M. Leblanc, G. Ferey, F. Varret, J. Magn. Magn. Mater. 43 (1984) 195.
[45] G.K. Wertheim, H.J. Guggenheim, D.N.E. Buchanan, Phys. Rev. 169 (1968) 465.
[46] S. Ramasamy, J. Jiang, H. Gleiter, R. Birringer, U. Gonser, Solid State Commun. 74 (1990) 851.
[47] P. Matteazzi, G. Le Caër, J. Alloys Compd. 187 (1992) 305.
[48] A.R. Denton, N.W. Ashcroft, Phys. Rev. A 43 (1991) 3161.
[49] N. Yamakawa, M. Jiang, B. Key, C.P. Grey, J. Am. Chem. Soc. 131 (2009) 10525.
[50] P.H. Christensen, S. Moerup, J.W. Niemantsverdriet, J. Phys. Chem. 89 (1985) 4898.
[51] F. Wang, R. Robert, N. a Chernova, N. Pereira, F. Omenya, F. Badway, X. Hua, M. Ruotolo, R. Zhang, L. Wu, V. Volkov, D. Su, B. Key, M.S. Whittingham, C.P. Grey, G.G. Amatucci, Y. Zhu, J. Graetz, J. Am. Chem. Soc. 133 (2011) 18828.
[52] A.V. Plakhotnyk, L. Ernst, R. Schmutzler, J. Fluor. Chem. 126 (2005) 27.
[53] M. Leblanc, J. Pannetier, G. Ferey, R. De Pape, Rev. Chim. Miner. 22 (1985) 107.
[54] J.M. Grenèche, F. Varret, in: G.J. Long, F. Grandjean (Eds.), Mössbauer Spectroscopy Applied to Magnetism and Materials Science, Springer US, Boston, MA, 1993, pp. 161–203.
[55] J. Chappert, J. Portier, Solid State Commun. 4 (1966) 185.
[56] N.N. Greenwood, A.T. Howe, F. Ménil, J. Chem. Soc. A Inorg. Phys. Theor. (1971) 2218.
[57] R.A. Brand, F. Hippert, B. Frick, J. Phys, Condens. Matter 21 (2009) 045405.